The wheeled three-link snake model: Singularities in nonholonomic constraints and stick-slip hybrid dynamics induced by Coulomb friction.

Tal Yona · Yizhar Or

Abstract The wheeled three-link snake model is a well-known example of an underactuated robotic system whose motion can be kinematically controlled by periodic changes of its internal shape, coupled with nonholonomic constraints. A known problem of this model is the existence of kinematic singularities at symmetric configurations where the three constraints become linearly dependent. Another critical assumption of this model is that the constraints of zero lateral slippage always hold, which requires large friction at the ground contact. This assumption breaks down when the inputs' actuation frequency becomes too large, or when passing through singular configurations where the constraint forces grow unbounded. In this work, we extend the kinematic model by allowing for wheels slippage when the constraint forces reach an upper bound imposed by Coulomb friction. Using numerical simulations, we analyze the system's hybrid dynamics governed by stick-slip transitions at the three wheels. We study the influence of actuation frequency on evolution of stick-slip periodic solutions which induce reversal in direction of net motion, and also show existence of optimal frequencies that maximize the net displacement per cycle or mean translational speed. In addition, we show that passing through kinematic singularities is overcome by stick-slip transitions which keep the constraint forces and body velocity at finite bounded values. The analysis proves that in some cases, simple kinematic models of underactuated robotic locomotion should be augmented by the
system's hybrid dynamics which accounts for realistic frictional bounds on contact forces.

1 Introduction

Kinematics and dynamics of mobile robotic locomotion is commonly studied within the framework of mechanical systems with nonholonomic constraints [1,2]. The motion of such systems is described by a set of generalized coordinates $\mathbf{q} \in I\!\!R^n$ and governed by k non-integrable constraints of the form $f_i(\mathbf{q}, \dot{\mathbf{q}}) = 0$ for $i = 1 \dots k$, or a more specific matrix form $\mathbf{W}(\mathbf{q})\dot{\mathbf{q}} = 0$. A classical example is the *Chaplygin's sleigh* [3,4], which contains a blade whose sliding motion is constrained to a specific body-fixed direction in the plane. Other common examples of nonholonomic systems are wheeled toy vehicles where the wheels' axles are assumed to maintain zero lateral slip (no-skid constraints), such as the snakeboard [5,6], roller racer [7,8] and more [9,10]. In most of theoretical models of such locomotion systems, it is assumed that the shape variables of the robot (e.g. internal joint angles) are directly prescribed as a control input, and typically undergoing time-periodic trajectories called *gaits* [11,12]. Nevertheless, there are few models which account for mechanical actuation of controlled internal torques or forces at the joints [13].

A key characteristic of locomotion systems is their under-actuation. This means that the number of control inputs m is smaller than the number of degrees-of-freedom n, leaving $n-m$ passive degrees of freedom. Assuming kinematic control of shape variables, if the number of nonholonomic constraints satisfies $k = n-m$, the motion of the system is completely determined by the inputs and the constraints, represented by a system of first-order ordinary differential equations (ODE). Such

T. Yona
Faculty of Mechanical Engineering, Technion - Israel Institute of Technology, Haifa 3200003, Israel

Y. Or (Corresponding Author), ORCID 0000-0002-9091-9357
Faculty of Mechanical Engineering, Technion - Israel Institute of Technology, Haifa 3200003, Israel.
Tel. +972 48295493, E-mail: izi@technion.ac.il

systems are called *kinematic systems*, and their net motion under a periodic gait input depend only on geometry and not on time-parametrization of the input. Examples of such systems are the kinematic snake model [14] and truck-trailers systems [15,16]. In case where there are fewer constraints, $k < n - m$, one also has to account for the dynamics of the system in order to determine its motion, which is no longer time-invariant, and governed by second-order ODE system. Examples of this case are the models of snakeboard [5], roller-racer [7] and twistcar [13].

Another branch in the literature on robotic locomotion models are multi-link swimmers [17], which are often also represented as kinematic control systems. For micro-scale swimmers in Stokes flow where drag forces are dominating, the nonholonomic constraints are induced by balance of net forces and torques in quasistatic motion [18]. For large inertia-driven swimmers in "inviscid" potential flow, the constraints originate from symmetries and momentum conservation laws [19,20]. Several works have studied geometric symmetries and gait planning for such systems [21,22], as well as gait optimization for maximizing various performance measures [23–25].

In mechanical control systems, the dynamics is commonly formulated using constrained Lagrange's equations, which contain terms of generalized forces that enforce the constraints [26]. For wheeled vehicles with no-slip constraints, such forces are generated by contact with the ground, and their magnitude is practically limited by friction bounds. In spite of this, most of the works in the literature assume ideal no-slip constraints without limitations. One possible extension that accounts for possible relaxation of the constraint is the "slip-angle" model, which enables lateral slip and assume a known relation between the constraint forces and the wheels' slip direction [27–30]. A slightly different model assumes viscous dissipation forces, which are linearly proportional to the slip velocity [31]. Both models result in smooth changes of slip velocity and constraint forces. On the other hand, the use of Coulomb's friction model induces nonsmooth transitions between slip and no-slip states. This model has been used in few works in order to study frictional stick-slip transitions in nonholonomic models of wheeled robot locomotion such as Chaplygin's sleigh [32], and the snakeboard [33].

Some works have used those models of wheel slippage in order to study motion planning and control of differentially driven wheeled mobile robots, for detecting and overcoming slippage [34–37]. Importantly, any model that incorporates wheel slippage turns the kinematic locomotion system into a dynamic one. The influence of actuation frequency on the system's behavior
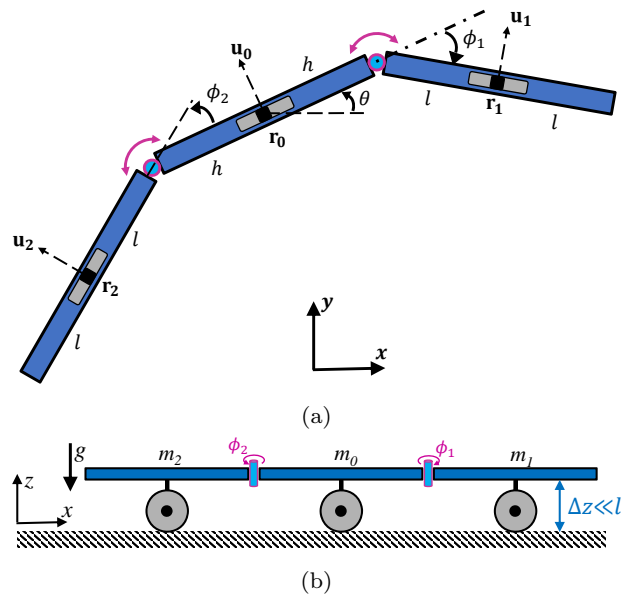

Fig. 1: The wheeled three-link snake model: (a) Top view (xy plane). (b) Side view.

and performance under periodic shape inputs has not been studied in previous works.

Snake-robot models typically consist of a chain of multiple rigid links connected by actuated joints. Such models have been vastly used in the past decades for describing the motion of snakes in nature, as well as the motion control of bio-inspired snake robots [38]. A key feature of terrestrial snake locomotion is exploiting anisotropy of frictional resistance in snake-ground contact in order to induce propulsion under periodic wavelike shape changes. Therefore, chains of robotic trailers with passive wheels have commonly been used in order to demonstrate snake locomotion, where frictional anisotropy is represented by no-skid nonholonomic constraints [39,40]. Our work focuses on the basic building block of those robotic snake-like wheeled chains, which is the model of *wheeled three-link (kinematic) snake*. This model consists of three links connected by two controlled joints and supported by three wheels, as shown in Figure 1. This is a classical kinematic system whose motion is determined by input of the two joint angles ϕ_1, ϕ_2, combined with three nonholonomic constraints of zero lateral slip at the wheels.

Several previous works have shown that the kinematic equations of the three-link kinematic snake have singularity at symmetric configurations where $\phi_1 = \phi_2$, for which the nonholonomic constraints become linearly dependent and the robot's body velocities may grow unbounded. In the work [14], symmetric gaits for this robot have been analyzed without accounting for the singularity. Nevertheless, simple robotic experiments re-

ported in [14] have indicated significant lateral slippage of the wheels near singular configurations, since the ground contact forces could not maintain the constraints due to friction bounds. Few works have added considerations of avoiding singularities for kinematic three-link and multi-linked wheeled robots [40–42]. More recent works have incorporated dynamic models for bypassing singularities of the kinematic snake, such as mechanically locking one joint at the singular configurations and adding gravity forces on a slope [43], or replacing one actuated joint by a passive torsion spring [44]. None of the works listed above have imposed friction bounds on the constraint force or studied stick-slip transitions near singular configurations.

The goal of this work is to revisit the model of the wheeled three-link kinematic snake robot and study its singular configurations, combined with hybrid dynamics under Coulomb's friction bounds and stick-slip transitions. First, we formulate the constrained dynamics of the system and show that constraint forces grow unbounded at singular configurations even for symmetric gaits where body velocities remain finite. Then we formulate the hybrid dynamics under transitions between stick-slip states of the wheels' contacts. Using numerical simulations, we first study the influence of actuation frequency of input on the robot's motion under a non-singular gait. We show that frictional stick-slip transitions break the time invariance and result in non-monotonic dependence on the frequency, that induces reversal in the direction of the robot's net motion. We obtain optimal frequencies for maximizing either the net displacement per cycle or the mean speed. Next, we study the motion under symmetric gaits that cross singular configurations, and show that slippage must occur at any actuation frequency and that the hybrid model ensures that constraint forces and body velocities always remain finite and bounded. Finally, we study the influence of gait's amplitude and compare between singular and non-singular gaits. Our analysis proves that the simple kinematic model should be augmented by the system's dynamics, and that Coulomb's friction law and stick-slip hybrid transitions resolve the system's kinematic singularity in a physically meaningful way.

2 Kinematic formulation and singularity analysis

The model of the wheeled three-link snake robot is shown in Figure 1. It has front-back symmetry, where lengths of middle link and side links are $2h$ and $2l$, respectively. A nondimensional length ratio is defined as $\eta = h/l$. Planar motion of the robot is described by the generalized coordinates $\mathbf{q} = (x, y, \theta, \phi_1, \phi_2)^T$. They are divided into shape coordinates $\mathbf{q}_s = (\phi_1, \phi_2)^T$, and body coordinates $\mathbf{q}_b = (x, y, \theta)^T$, where x, y denote the position of the center point $\mathbf{r}_0$ of the middle link, and θ is its orientation angle. The shape coordinates, i.e. joint angles ϕ_1, ϕ_2, are assumed to be directly actuated and controlled, whereas the body motion evolves indirectly and passively due to shape actuation. The mechanism which connects between shape and body motion is the nonholonomic constraints induced by assuming no lateral slippage (skid) of the three wheels. Let $\mathbf{r}_i$ denote the position of the ith wheel's axle, for $i = \{0, 1, 2\}$. Their positions are given by

$$\mathbf{r}_0 = \begin{pmatrix} x \\ y \end{pmatrix}, \ \mathbf{r}_1 = \mathbf{r}_0 + h \begin{pmatrix} \cos\theta \\ \sin\theta \end{pmatrix} + l \begin{pmatrix} \cos(\theta - \phi_1) \\ \sin(\theta - \phi_1) \end{pmatrix}$$
$$\mathbf{r}_2 = \mathbf{r}_0 - h \begin{pmatrix} \cos\theta \\ \sin\theta \end{pmatrix} - l \begin{pmatrix} \cos(\theta + \phi_2) \\ \sin(\theta + \phi_2) \end{pmatrix}.$$
$$(1)$$

Each wheel axle is constrained to move only along the link's longitudinal direction without slipping laterally. The lateral directions of each wheel axle $\mathbf{u}_i$ are given by

$$\mathbf{u}_0 = \begin{pmatrix} -\sin\theta \\ \cos\theta \end{pmatrix}, \ \mathbf{u}_1 = \begin{pmatrix} -\sin(\theta - \phi_1) \\ \cos(\theta - \phi_1) \end{pmatrix},$$
$$\mathbf{u}_2 = \begin{pmatrix} -\sin(\theta + \phi_2) \\ \cos(\theta + \phi_2) \end{pmatrix}.$$
$$(2)$$

The no-slip constraints are $\dot{\mathbf{r}}_i \cdot \mathbf{u}_i = 0$. They can be written in terms of vector $\dot{\mathbf{q}}$ of generalized velocities as

$$v_i = \dot{\mathbf{r}}_i \cdot \mathbf{u}_i = \mathbf{w}_i(\mathbf{q}) \cdot \dot{\mathbf{q}} = 0 \text{ for } i = \{0, 1, 2\}. \quad (3)$$

Grouping the three equations in (3), the no-slip nonholonomic constraints are obtained in matrix form as:

$$\mathbf{W}(\mathbf{q})\dot{\mathbf{q}} = 0,$$

where $\mathbf{W}(\mathbf{q}) =$

$$\begin{pmatrix} -\sin\theta & \cos\theta & 0 & 0 & 0 \\ \sin(\phi_1 - \theta) & \cos(\phi_1 - \theta) & h\cos(\phi_1) + l & -l & 0 \\ -\sin(\phi_2 + \theta) & \cos(\phi_2 + \theta) & -h\cos(\phi_2) - l & 0 & -l \end{pmatrix}$$
$$(4)$$

The constraint matrix in (4) can be decomposed into blocks related to body and shape velocities $\mathbf{W} = (\mathbf{W}_b \ \mathbf{W}_s)$, which gives

$$\mathbf{W}_b(\mathbf{q})\dot{\mathbf{q}}_b + \mathbf{W}_s\dot{\mathbf{q}}_s = 0. \quad (5)$$

Since (5) contains three scalar constraints and three body velocities, it can be inverted in order to obtain

$$\dot{\mathbf{q}}_b = -\mathbf{W}_b(\mathbf{q})^{-1}\mathbf{W}_s\dot{\mathbf{q}}_s. \quad (6)$$
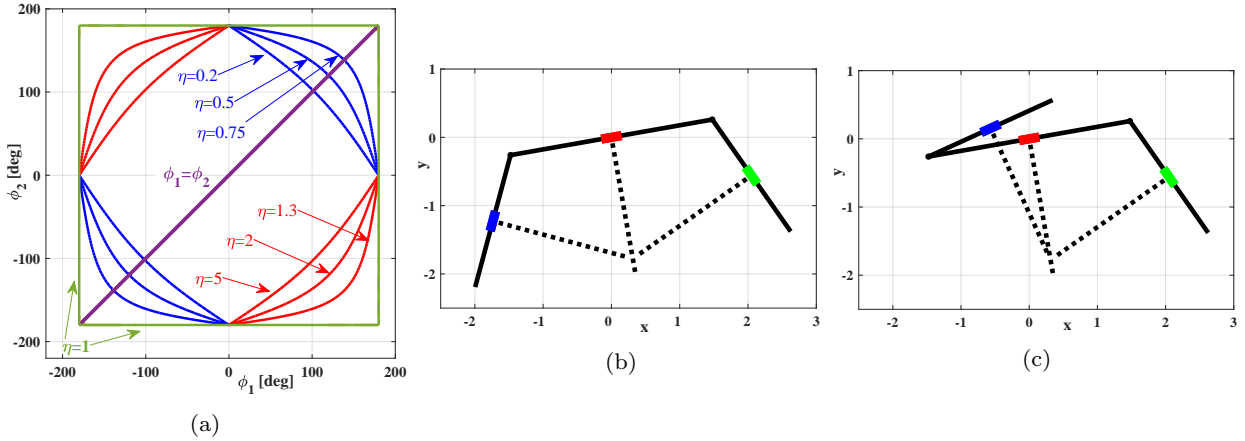
Fig. 2: (a) Curves of singular configurations in (ϕ_1, ϕ_2)-plane; Two singular configurations for $\eta = h/l = 1.5$ and $\phi_1 = 65°$: (b) Symmetric $\phi_2 = 65°$, and (c) Asymmetric $\phi_2 = 194.5°$

The first-order nonlinear system in (6) is the kinematic equation which governs the robot's body motion $\mathbf{q}_b(t)$ for a given input of shape changes $\mathbf{q}_s(t)$. For a periodic input of shape changes (gait), one only needs to integrate (6) over a single period, due to invariance of the system's constraints with respect to rigid-body transformations (gauge symmetry, cf. [11,5]). Additionally, the system (6) is time-invariant, hence the robot's net motion in a period depends only on the chosen trajectory of $\mathbf{q}_s(t)$ in the shapes' space, and not on its time rate.

A major problem in the kinematic control of the three-link snake is the existence of singular configurations. Mathematically, this phenomenon is manifested by singularity of the constraint matrix $\mathbf{W}_b(\mathbf{q})$ in (6). The singularity condition is simply vanishing of the determinant of $\mathbf{W}_b$, which is given by:

$$\det(\mathbf{W}_b) = h\sin(\phi_2 - \phi_1) + l(\sin\phi_2 - \sin\phi_1) = 0. \quad (7)$$

An obvious solution of (7) is $\phi_1 = \phi_2$, which is a symmetric configuration of the robot. However, there also exists an additional curve of non-symmetric singular solutions. A plot of the singular curves in (ϕ_1, ϕ_2) plane is shown in Figure 2a, for several values of links' length ratio $\eta = h/l$. It can be seen that the line of symmetric singular solution $\phi_1 = \phi_2$ always exists, whereas the additional singular curves depend on the value of η, and undergo a qualitative change between cases of $\eta < 1$ and $\eta > 1$. In the limiting case of $\eta = 1$, where all robot's links are equal, those curves reduce to $\phi_i = \pm\pi$ for $i = 1$ or $i = 2$. Such configurations, in which the links are folded on each other, are generally not physical due to inter-collision between the links. Since most of previous works focused on the case of equal links $\eta = 1$, the non-symmetric singular configurations have

not been previously considered. Figures 2b-2c show illustration of the two singular configurations of the robot for $\phi_1 = 65°$ and $\eta = 1.5$. The symmetric configuration in which $\phi_2 = \phi_1$ appears in Figure 2b, while the non-symmetric singular configuration where $\phi_2 = 194.5°$ appears in Figure 2c. The geometric interpretation of singular configurations is clear from both examples: the lines of the three axles intersect at a common point. This implies that when the joint angles are held fixed, the robot is not immobilized and can move by rigidly rotating about the intersection point.

When the robot's shape $\mathbf{q}_s$ approaches a singular configuration, the kinematic equation (6) generally implies that the body velocities $\dot{\mathbf{q}}_b$ grow unbounded. However, there are special cases in which $\dot{\mathbf{q}}_b$ can remain finite and bounded while crossing a singular configuration. This occurs in cases where $\mathbf{W}_s\dot{\mathbf{q}}_s$ lies precisely in the linear subspace spanned by the columns of the (rank-deficient) singular matrix $\mathbf{W}_b(\mathbf{q})$ in (6). Using (4) and (5) leads to the condition:

$$\dot{\phi}_1 \sin\phi_2 + \dot{\phi}_2 \sin\phi_1 = 0. \quad (8)$$

In particular, for the symmetric singular configurations $\phi_1 = \phi_2$, the condition (8) simply reduces to $\dot{\phi}_1 = -\dot{\phi}_2$. Geometrically, this means that the shape trajectory in (ϕ_1, ϕ_2) plane crosses the singularity line $\phi_1 = \phi_2$ precisely at a perpendicular direction.

In this work, we consider periodic gaits where the joint angles $\mathbf{q}_s(t)$ are given by harmonic functions as:

$$\phi_1(t) = \alpha_1 + \beta_1\sin(\omega t), \ \phi_2(t) = \alpha_2 + \beta_2\cos(\omega t). \quad (9)$$

In order to demonstrate the different behavior while crossing the singularity lines, two cases are considered where $\alpha_1 = \alpha_2 = 0$ in both of them: a circular gait where $\beta_1 = \beta_2 = 0.3\pi$, and an elliptic gait where
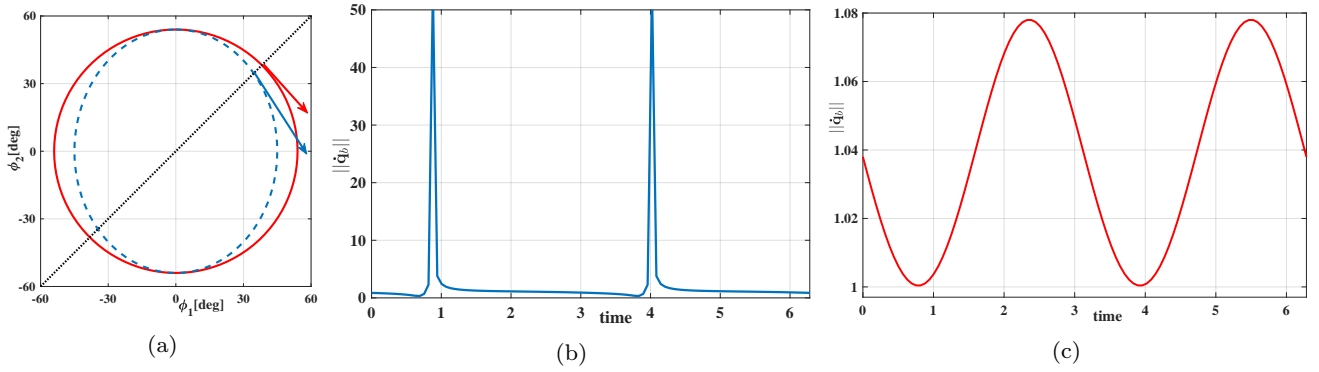
Fig. 3: (a) Circular (solid) and elliptic (dashed) gait trajectories in (ϕ_1, ϕ_2)-plane. Time-plots of the norm of body velocities $||\dot{\mathbf{q}}_b(t)||$: (b) For the elliptic gait. (c) For the circular gait.

$\beta_1 = 0.25\pi$ and $\beta_2 = 0.3\pi$. The two gaits are shown in Figure 3a in (ϕ_1, ϕ_2)-plane. It can be seen that the circular gait satisfies the condition $\dot{\phi}_1 = -\dot{\phi}_2$ at the singularity line $\phi_1 = \phi_2$ (dotted line), while this is not satisfied by the elliptical gait. Figures 3b,3c show time plots of the norm of body velocity $||\dot{\mathbf{q}}_b(t)||$ along a period of both gaits, calculated according to (6) and (9) for $\omega = 1 \ rad/s$. (Linear and angular velocities are normalized by $l\omega$ and ω, respectively). It can be seen that the body velocity grows unbounded upon crossing the singularity line under the elliptical gait, but stays finite and bounded under the circular gait. In the next section, we show that even in this case where kinematic singularity is overcome, the constraint forces may still grow unbounded.

3 Dynamic analysis under ideal no-slip constraints

We now formulate the dynamic equations of motion and show how constraint forces can be computed. We use the standard formulation of constrained Lagrange's equations [26], explained as follows. Consider a system with generalized coordinates $\mathbf{q} \in I\!\!R^n$ where n is the number of degrees of freedom. The system is subject to k nonholonomic constraints of the form $\mathbf{W}(\mathbf{q})\dot{\mathbf{q}} = 0$ where $\mathbf{W} \in I\!\!R^{k \times n}$. The dynamic equations of motion of the constrained system are given:

$$\frac{d}{dt}\left(\frac{\partial L}{\partial \dot{\mathbf{q}}}\right) - \frac{\partial L}{\partial \mathbf{q}} = \mathbf{F}_q + \mathbf{W}(\mathbf{q})^T \mathbf{\Lambda}, \tag{10}$$

where $L = T - U$ is the system's Lagrangian, T is the total kinetic energy, U is the potential energy, $\mathbf{F}_q$ is the vector of generalized forces and $\mathbf{\Lambda} \in I\!\!R^k$ is the vector of constraint forces (Lagrange multipliers). Since the robot here moves in horizontal plane, our system is not governed by any changes in potential energy and U can

thus be ignored. The total kinetic energy for planar motion of N rigid bodies can be obtained as

$$T = \frac{1}{2}\sum_{i=1}^{N}\left(m_i(\dot{\mathbf{r}}_i \cdot \dot{\mathbf{r}}_i) + I_i\omega_i^2\right), \tag{11}$$

where m_i is the mass of link i, $\dot{\mathbf{r}}_i$ is its center-of-mass velocity, I_i is its moment of inertia, and ω_i is its angular velocity. We assume for convenience that all robot's links are uniform rods such that $I_0 = m_i h^2/3$ and $I_1 = I_2 = m_i l^2/3$. Moreover, all rods have equal diameter and density, so that the links' masses are related as $m_0 = \eta m_1 = \eta m_2$. The links' center-of-mass positions are given in (1), and their angular velocities are given by

$$\omega_0 = \dot{\theta}, \ \omega_1 = \dot{\theta} - \dot{\phi}_1, \ \omega_2 = \dot{\theta} + \dot{\phi}_2. \tag{12}$$

Using all the assumptions above, the equations of motion can be obtained using (10) and (11), and can be written in a standard matrix form as

$$\mathbf{M}(\mathbf{q})\ddot{\mathbf{q}} + \mathbf{B}(\mathbf{q}, \dot{\mathbf{q}}) = \mathbf{E}\boldsymbol{\tau} + \mathbf{W}(\mathbf{q})^T\mathbf{\Lambda}$$

$$\text{where } \mathbf{E} = \begin{pmatrix} 0\ 0\ 0\ 1\ 0 \\ 0\ 0\ 0\ 0\ 1 \end{pmatrix}^T, \ \mathbf{\Lambda} = (\lambda_0, \lambda_1, \lambda_2)^T, \tag{13}$$

and $\boldsymbol{\tau} = (\tau_1, \tau_2)^T$ is the vector of actuation torques at the joints. The structure of the matrix $\mathbf{E}$ on the right hand side of (13) indicates the under-actuation of the system, since the shape coordinates $\mathbf{q}_s$ are directly actuated whereas the body coordinates $\mathbf{q}_b$ are not. On the left hand side of (13), explicit expressions of inertia matrix $\mathbf{M}(\mathbf{q})$ and vector of velocity-dependent terms $\mathbf{B}(\mathbf{q}, \dot{\mathbf{q}})$ are given in Table 1.

The matrices $\mathbf{M}(\mathbf{q}), \mathbf{B}(\mathbf{q}, \dot{\mathbf{q}}), \mathbf{W}(\mathbf{q})$ in (13) can be decomposed into blocks corresponding to body and shape coordinates $\mathbf{q}_b, \mathbf{q}_s$ as follows:

$$\begin{bmatrix} \mathbf{M}_{bb}\ \mathbf{M}_{bs} \\ \mathbf{M}_{bs}^T\ \mathbf{M}_{ss} \end{bmatrix}\begin{pmatrix} \ddot{\mathbf{q}}_b \\ \ddot{\mathbf{q}}_s \end{pmatrix} + \begin{pmatrix} \mathbf{B}_b \\ \mathbf{B}_s \end{pmatrix} = \begin{pmatrix} 0 \\ \boldsymbol{\tau} \end{pmatrix} + \begin{pmatrix} \mathbf{W}_b^T \\ \mathbf{W}_s^T \end{pmatrix}\mathbf{\Lambda}. \tag{14}$$

$$\mathbf{M}(\mathbf{q}) = m_1 \begin{pmatrix} \eta+2 & 0 & l(s_1+s_2) & -ls_1 & ls_2 \\ 0 & \eta+2 & l(c_1-c_2) & -lc_1 & -lc_2 \\ l(s_1+s_2) & l(c_1-c_2) & \frac{l^2}{3}(6\eta(\cos\phi_1+\cos\phi_2)+\eta^3+6\eta^2+8) & -\frac{l^2}{3}(3\eta\cos\phi_1+4) & \frac{l^2}{3}(3\eta\cos\phi_2+4) \\ -ls_1 & -lc_1 & -\frac{l^2}{3}(3\eta\cos\phi_1+4) & \frac{4}{3}l^2 & 0 \\ ls_2 & -lc_2 & \frac{l^2}{3}(3\eta\cos\phi_2+4) & 0 & \frac{4}{3}l^2 \end{pmatrix}$$

$$\mathbf{B}(\mathbf{q},\dot{\mathbf{q}}) = m_1 l \begin{pmatrix} \dot{\theta}^2(c_2-c_1)-\dot{\phi}_1^2c_1+\dot{\phi}_2^2c_2+2\dot{\theta}(\dot{\phi}_1c_1+\dot{\phi}_2c_2) \\ \dot{\theta}^2(s_1+s_2)+\dot{\phi}_1^2s_1+\dot{\phi}_2^2s_2+2\dot{\theta}(\dot{\phi}_2s_2-\dot{\phi}_1s_1) \\ -l\eta(2\dot{\theta}(\dot{\phi}_1s_1+\dot{\phi}_2s_2)+\dot{\phi}_2^2s_2-\dot{\phi}_1^2s_1) \\ l\eta\dot{\theta}^2s_1 \\ l\eta\dot{\theta}^2s_2 \end{pmatrix}$$

where $c_1 = \cos(\phi_1-\theta)$, $s_1 = \sin(\phi_1-\theta)$, $c_2 = \cos(\phi_2+\theta)$, $s_2 = \sin(\phi_2+\theta)$.

Table 1: Expressions of $\mathbf{M}(\mathbf{q})$ and $\mathbf{B}(\mathbf{q},\dot{\mathbf{q}})$ in Eq. (13)

In the case of a mechanical control, the joint torque vector $\boldsymbol{\tau}(t)$ is prescribed while the body and shape variables $\mathbf{q}_b(t), \mathbf{q}_s(t)$ are dynamically evolving. On the other hand, in the case of kinematic control considered here, the shape variables $\mathbf{q}_s(t)$ are prescribed while the joint torques $\boldsymbol{\tau}(t)$ are determined and the body variables $\mathbf{q}_b(t)$ are dynamically evolving. In both cases, additional information is required for obtaining the unknown constraint forces $\boldsymbol{\Lambda}$ in (13). This information is obtained by differentiation of the nonholonomic constraint (4) with respect to time. Using that $\dot{\mathbf{W}}_s = 0$, this gives

$$\mathbf{W}(\mathbf{q})\ddot{\mathbf{q}} + \dot{\mathbf{W}}(\mathbf{q},\dot{\mathbf{q}})\dot{\mathbf{q}} = \mathbf{W}_b\ddot{\mathbf{q}}_b + \mathbf{W}_s\ddot{\mathbf{q}}_s + \dot{\mathbf{W}}_b\dot{\mathbf{q}}_b = 0. \quad (15)$$

Combining equations (14) and (15) gives a linear system in the unknowns $(\ddot{\mathbf{q}}_b, \boldsymbol{\tau}, \boldsymbol{\Lambda})$ for a prescribed shape input given by a function $\mathbf{q}_s(t)$ with known derivatives, as:

$$\underbrace{\begin{pmatrix} \mathbf{M}_{bb} & \mathbf{0} & -\mathbf{W}_b^T \\ \mathbf{M}_{bs}^T & -\mathbf{I}_2 & -\mathbf{W}_s^T \\ \mathbf{W}_b & \mathbf{0} & \mathbf{0} \end{pmatrix}}_{\mathbf{A}_{8\times 8}} \begin{pmatrix} \ddot{\mathbf{q}}_b \\ \boldsymbol{\tau} \\ \boldsymbol{\Lambda} \end{pmatrix} = \begin{pmatrix} -\mathbf{M}_{bs}\ddot{\mathbf{q}}_s - \mathbf{B}_b \\ -\mathbf{M}_{ss}\ddot{\mathbf{q}}_s - \mathbf{B}_s \\ -\mathbf{W}_s\ddot{\mathbf{q}}_s - \dot{\mathbf{W}}_b\dot{\mathbf{q}}_b \end{pmatrix},$$
$$(16)$$

where $\mathbf{I}_2$ is a 2×2 identity matrix and $\mathbf{0}$ denotes zero blocks of compatible dimensions. The 8×8 matrix $\mathbf{A}$ in (16) has to be inverted in order to find the dynamic solution for the unknowns $(\ddot{\mathbf{q}}_b, \boldsymbol{\tau}, \boldsymbol{\Lambda})$. Direct (yet a bit tedious) calculation shows that the determinant of $\mathbf{A}$ satisfies

$$\det(\mathbf{A}) = \det(\mathbf{W}_b)^2 = [h\sin(\phi_2-\phi_1)+l(\sin\phi_2-\sin\phi_1)]^2. \quad (17)$$

This implies that the dynamic solution of (16) under kinematic control reaches a singularity whenever the kinematic system is singular. As an example, we revisit the case of a circular gait (9) where $\beta_1 = \beta_2 = 0.3\pi$ and $\omega = 1 rad/s$. This gait has already been considered in the kinematic analysis in the previous section, and it has been shown that it overcomes the kinematic singularity while maintaining bounded body velocity. We now substitute $\mathbf{q}_s(t)$ and its derivatives into the dynamic equation (16). Physical parameters of the robot are chosen as $l = h = 0.1m$ and $m_0 = m_1 = m_2 = 0.17Kg$. Initial body position is chosen as $\mathbf{q}_b(0) = 0$ while initial body velocities $\dot{\mathbf{q}}_b(0)$ are obtained by substituting the given $\mathbf{q}_s(0), \dot{\mathbf{q}}_s(0)$ into the nonholonomic constraints (4). The constraint forces $\lambda_0, \lambda_1, \lambda_2$ and the actuation torques τ_1, τ_2 are plotted in Figures 4a and 4b as a function of time, zoomed in around $t = 0.7854$ when the singular configuration $\phi_1 = \phi_2$ is crossed. It can be seen that these forces and torques both grow unbounded near the singular configurations. This is in spite of the fact that the body velocities remain bounded (see Figure 3c) since the gait satisfies the relation (8). Thus, it is concluded that one can overcome the kinematic singularity at velocity level, but not the dynamic singularity at force and torque level.

Next, we consider dynamic simulation for a shifted circular gait that does not cross any singular configuration. This gait is obtained by choosing $\alpha_2 = -\alpha_1 = 0.2\pi$ and $\beta_1 = \beta_2 = 0.1\pi$. The gait is plotted in Figure 5a in (ϕ_1, ϕ_2)-plane, and one can see that it does not cross the singularity line $\phi_1 = \phi_2$ (dashed). Finding the motion of the robot can be done by integrating the kinematic equation (6). Figure 5b shows the trajectory of the robot's centerpoint $\mathbf{r}_0(t)$ during 7 periods of the gait. Animation movie of the simulated robot's motion appears in the supplementary information. The middle link's center makes a net displacement of $\Delta d = 0.52l$ in a period. Nevertheless, it can be seen that the net rotation of the robot in a cycle cancels out, so that the net
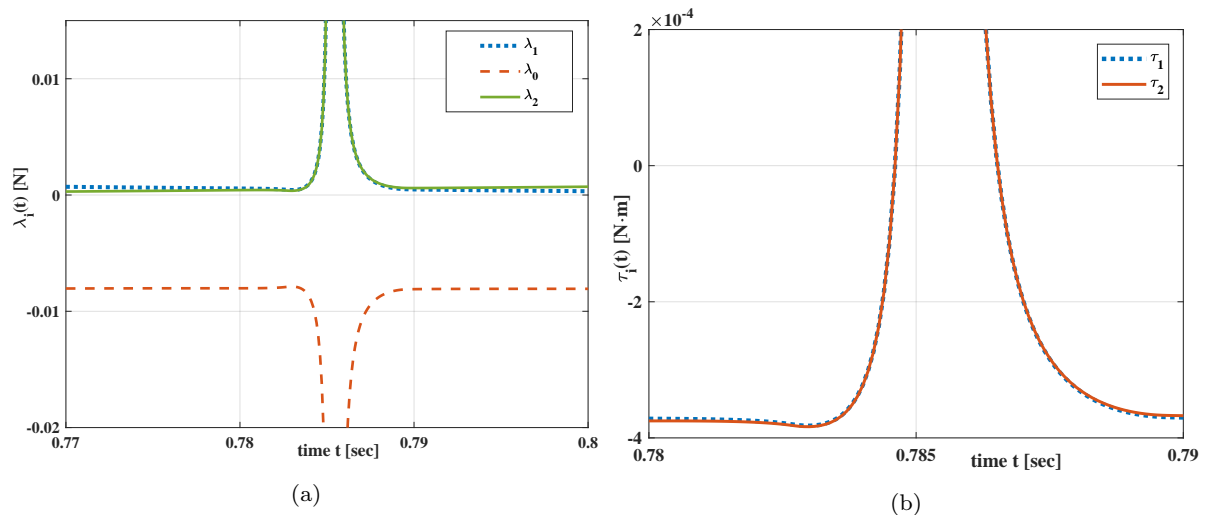
(a)

(b)

Fig. 4: Simulation results of the dynamics under circular gait: (a) Constraint forces $\lambda_i(t)$ for $i = 0, 1, 2$. (b) Actuation torques at joints $\tau_1(t), \tau_2(t)$.
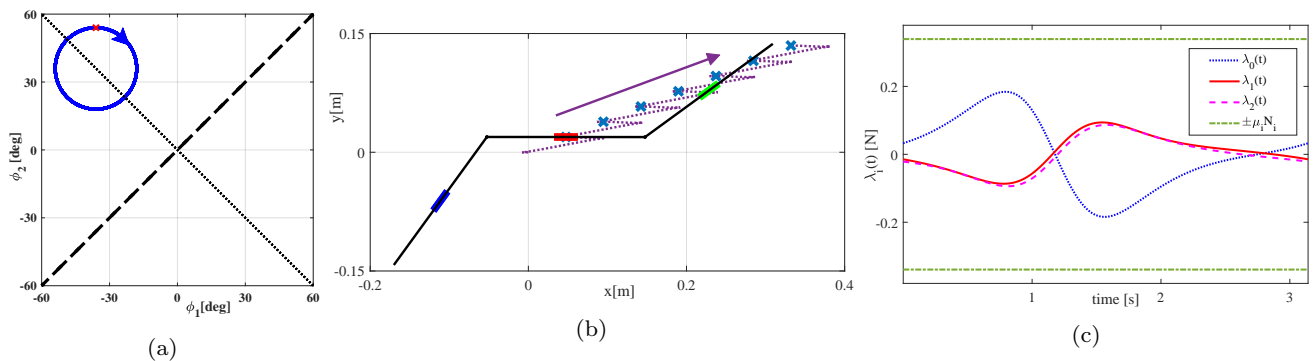

(a)

(b)

(c)

Fig. 5: (a) The shifted circle gait in (ϕ_1, ϕ_2)-plane. Simulation results for $\omega = 2rad/s$:(b) Trajectory of the robot's center $\mathbf{r}_0(t)$ (dotted curve), positions at integer period times are marked by '×'. (c) Constraint forces $\lambda_i(t)$ during a period. Dash-dotted horizontal lines are friction bounds $\pm\mu_i N_i$ discussed in Section 4.

motion is of pure translation. This is due to symmetry of the gait with respect to the skew line $\phi_1 = -\phi_2$. The constraint forces $\lambda_i(t)$ under this gait can be computed using Eq. (16), and the results are shown in Figure 5c for actuation frequency of $\omega = 2rad/s$. It can be seen that the constraint forces remain bounded. However, using dimensional analysis of the dynamic equations, it is proven in Appendix A that the constraint forces $\lambda_i(t)$ scale as ω^2 with the actuation frequency. Physically, the constraint forces are limited in practice by friction bounds. Therefore, increasing the actuation frequency ω beyond some critical value causes $\lambda_i(t)$ to reach their upper bounds. This, in turn, results in evolution of slippage, as studied in the next section.

4 Hybrid dynamics under friction bounds and stick-slip transitions

We now formulate the system's hybrid dynamics which accounts for friction bounds and stick-slip transitions. First, consider the case where the no-slip constraint (3) at the ith wheel axle is satisfied. The constraint force λ_i, which is a tangential force applied by the ground contact, must satisfy Coulomb's dry friction inequality:

$$|\lambda_i| \le \mu_i N_i \ , \ v_i = \mathbf{w}_i \cdot \dot{\mathbf{q}} = 0, \tag{18}$$

where μ_i is the coefficient of Coulomb's friction of the ith wheel with the ground and N_i is the normal reaction force at the wheel's axle. When the magnitude of λ_i reaches the bound in (18), lateral slip of the ith wheel begins to evolve. In such case, the magnitude of the corresponding constraint force stays at the maximal

bound and opposes the slip direction:

$$\lambda_i = -\mu_i N_i \mathrm{sgn}(v_i) \text{ where } v_i = \mathbf{w}_i \cdot \dot{\mathbf{q}} \neq 0. \tag{19}$$

For simplicity of the analysis, we do not distinguish between static and kinetic friction coefficients throughout this work. Another simplifying assumption is that the normal reaction forces at the wheels are constant, and their values are $N_i = m_i g$ for $\{0, 1, 2\}$, where g is the gravitational acceleration. This can be justified if each wheel axle is located at the middle of the link, as shown in the side view in Figure 1b. Moreover, it is also assumed that the center-of-mass of each link is located very low above the ground $\Delta z \ll l$, so that its acceleration has negligible contribution to the normal reaction force.

The stick-slip states described above lead to $2^3 = 8$ possible "modes" – combinations of the three wheels' stick-slip states. The dynamic equations of each mode is governed by a different set of equations, described as follows. First, the constrained Lagrange equations (14) still hold, which gives 5 scalar equations. However, the equation (15) of the time-derivative of the no-slip constraints should be replaced by three equations which depend on the slip state of each wheel, given as:

$$\begin{cases} \mathbf{w}_i(\mathbf{q}) \cdot \ddot{\mathbf{q}} + \dot{\mathbf{w}}_i(\mathbf{q}, \dot{\mathbf{q}}) \cdot \dot{\mathbf{q}} = 0 & \text{wheel } i \text{ is not slipping} \\ \lambda_i = -\mu_i N_i \mathrm{sgn}(\mathbf{w}_i(\mathbf{q}) \cdot \dot{\mathbf{q}}) & \text{wheel } i \text{ is slipping} \end{cases} \tag{20}$$

for $i = 0, 1, 2$. Combining equations (20) with (14) gives a linear systems in the unknowns $(\ddot{\mathbf{q}}_b, \boldsymbol{\tau}, \boldsymbol{\Lambda})$ for a prescribed shape input $\mathbf{q}_s(t)$, similar to equation (16).

Singularity of the hybrid dynamic equations should also be examined by constructing the matrix of the linear system which governs the dynamics under each mode of slip states and checking whether its determinant can cross zero. The detailed derivation of this singularity analysis appears in Appendix B. In summary, under the mode which includes slippage of wheel 0 only, the dynamics is singular for joint angles that satisfy $\phi_1 + \phi_2 = \pm\pi$ or for $\phi_1, \phi_2 = \pm\pi$. The latter case is non-physical since it involves inter-collision between links. Under the mode which includes slippage of wheel 1 or 2 only, the dynamics is singular only if the links lengths are equal, $\eta = 1$, for joint angles that satisfy $\phi_1 = \pm\pi$ or $\phi_2 = \pm\pi$. All other modes that involve slippage in two or more wheels turn out to be always non-singular.

The transitions between different modes of the hybrid dynamics are described as follows. A non-slipping wheel begins to slip whenever its constraint forces reaches its frictional bound, $|\lambda_i| = \mu_i m_i g$. When the slip velocity of a slipping wheel vanishes $\mathbf{w}_i(\mathbf{q}) \cdot \dot{\mathbf{q}} = 0$, the wheel may switch back to no-slip state, provided that the constraint force at the initial instant right after switching satisfies its bound $|\lambda_i| \leq \mu_i m_i g$. Otherwise, the wheel's slip velocity reverses its sign.

5 Numerical analysis of the kinematic snake's hybrid dynamics

In this section we present numerical simulations of the robot under hybrid stick-slip transitions. The simulations have been conducted using **ode45** procedure of **MATLAB** for adaptive-step integration, with event function for detection of mode transitions. Physical parameters are chosen as $l = h = 0.1m$ and $m_0 = m_1 = m_2 = 0.17Kg$, and friction coefficients of $\mu_0 = \mu_1 = \mu_2 = 0.2$.

5.1 Analysis of the shifted circle gait

We revisit the gait of shifted circle which has been analyzed in Section 3 under ideal no-slip constraints. The gait, which is plotted in Figure 5a, is defined by equation (9) with $\alpha_2 = -\alpha_1 = 0.2\pi$ and $\beta_1 = \beta_2 = 0.1\pi$. The constraint forces $\lambda_i(t)$ under actuation frequency of $\omega = 2rad/s$ were plotted in Figure 5c. It can be seen that the no-slip constraints can hold since all forces $\lambda_i(t)$ lie within the friction limits $\pm\mu_i m_i g$, denoted as the dash-dotted horizontal lines. However, since the constraint forces λ_i scale as ω^2, increasing the actuation frequency in (9) will result in evolution of stick-slip state transitions. Specifically, for $\omega > 2.7 \, rad/s$, the constraint force $\lambda_0(t)$ of the middle link's wheel reaches its friction bound and the wheel begins to slip. As an example, we simulate the robot's hybrid dynamics for $\omega = 3.6 \, rad/s$. Time plots of the constraint forces $\lambda_i(t)$ and of the slip velocity $v_0(t) = \mathbf{w}_0 \cdot \dot{\mathbf{q}}$ appear in Figures 6a and 6b, respectively. It can be seen that the central wheel 0 undergoes transitions of stick↔slip and slip reversal whereas the side wheels 1,2 do not slip at all. Animation movie of the simulated robot's motion appears in the supplementary information, where the blinking red arrow denotes times and direction of wheel slippage. One can notice the slight curvature of the robot's motion trajectory. The middle link's center makes a net displacement of $\Delta d = 0.54l$, while the link undergoes a net rotation of $\Delta\theta = 0.0273rad$ in a period. The reason for this rotation is the violation of symmetry which is induced by slippage, as can clearly be seen in slip velocity $v_0(t)$ which is not symmetric about zero and has nonzero mean. (Same holds for the constraint forces $\lambda_i(t)$, compare Figures 5c and 6a). The approx-
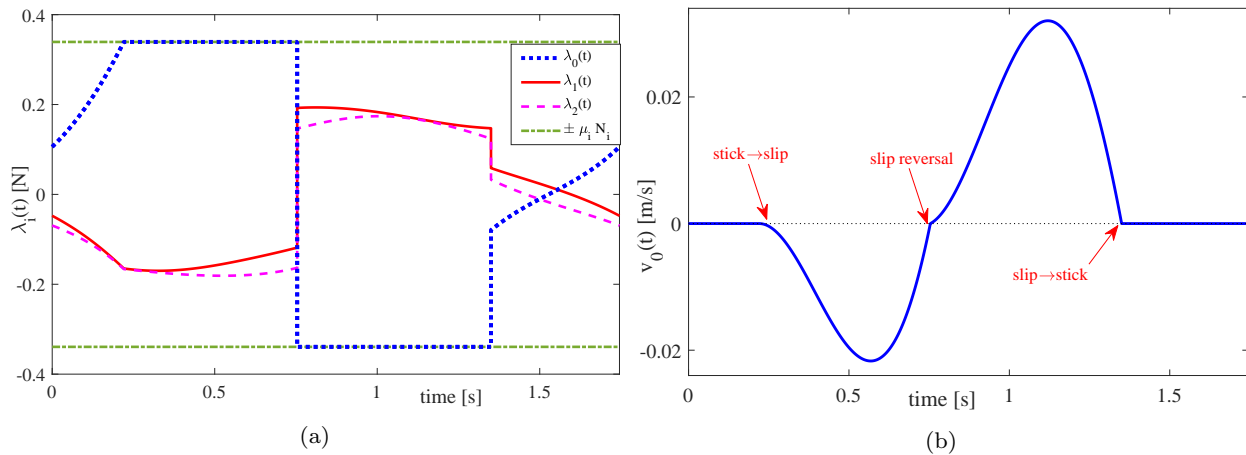
Fig. 6: Time plots of simulation results for the shifted circle gait with $\omega = 3.6\,rad/s$: (a) Constraint forces $\lambda_i(t)$. (b) Slip velocity $v_0(t)$.
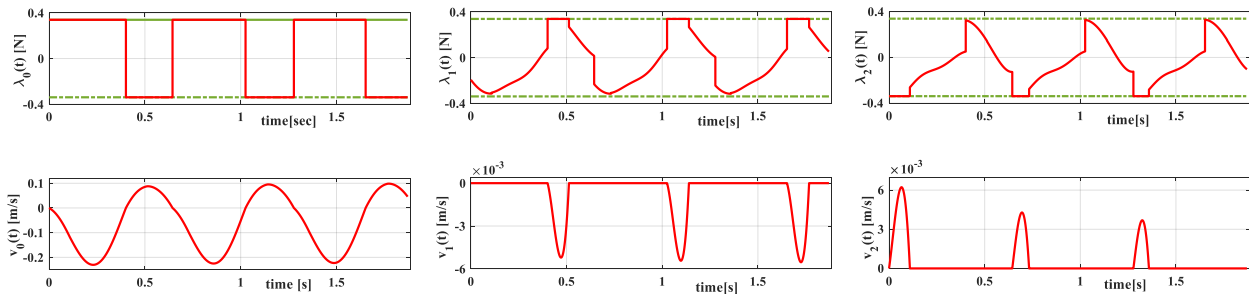

Fig. 7: Time plots of simulation results for the shifted circle gait with $\omega = 10\,rad/s$, constraint forces $\lambda_i(t)$ and slip velocities $v_i(t)$.

imate discrete radius of curvature of the trajectory is $\rho = \Delta d / \Delta \theta = 19.6l$.

Next, we simulate the robot's hybrid dynamics for a higher frequency of $\omega = 10\ rad/s$. Time plots of the constraint forces $\lambda_i(t)$ and slip velocities $v_i(t)$ appear in Figure 7. Importantly, since the simulation assumes initial conditions of zero slip velocities, the solution involves a transient phase followed by asymptotic convergence to periodic motion. In this simulation, the solution converges rapidly to periodic motion after approximately three periods. The middle link's center makes a net displacement of $\Delta d = 0.37l$ per period, while the link undergoes a net rotation of $\Delta \theta = 0.0161 rad$. It can be seen in the time plots that the periodic solution involves stick-slip transitions of the side wheels 1 and 2 while the central wheel 0 undergoes slip reversal transitions only. Any contact transition in one wheel may induce discontinuity and non-smoothness in the constraint forces and slip velocity of other wheels. Figure 8 shows the trajectory of the robot's centerpoint $\mathbf{r}_0(t)$ during several periods of the gait. Animation movie of the simulated robot's motion appears in the supplemen-
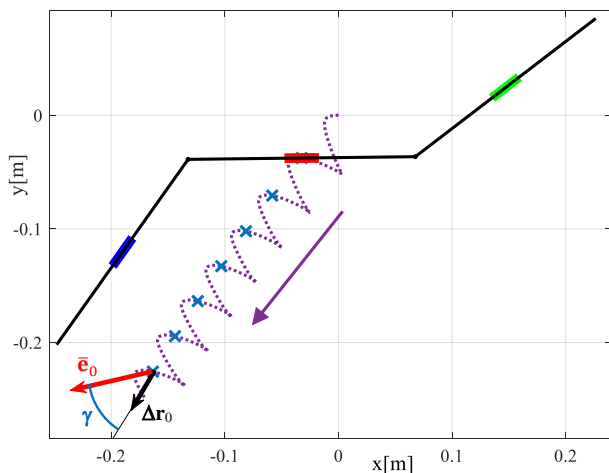

Fig. 8: Trajectory of the robot's center $\mathbf{r}_0(t)$ (dotted curve) under the shifted circle gait for $\omega = 10\,rad/s$. Positions at integer period times are marked by '$\times$'. Arrows denote the vectors $\Delta\mathbf{r}_0, \bar{\mathbf{e}}_0$.

tary information, where the colored blinking arrows denote times and direction of slippage at each wheel. Remarkably, one can see that the direction of net motion is reversed. That is, the robot moves to the left whereas in the lower frequencies ($\omega = 2, 3.6$) it moved to the right, for exactly the same gait, (see Figure 5b and supplementary movies). This frequency-dependent effect is further examined below.

We now study the influence of varying the actuation frequency ω of the input on the gait's performance. We conduct numerical simulations while the frequency varies within the range $2 \leq \omega \leq 10 rad/s$. At each frequency, different quantities of the periodic solution are calculated after passing the transient phase and convergence to periodic motion. Figure 9a plots the percentage of slipping time of each wheel in a period, as a function of frequency. It can be seen that there is no slippage for $\omega < 2.7 rad/s$, and that for $\omega > 9.4 rad/s$ all wheels are slipping. Figures 9b and 9c plot the net displacement per period Δd and the mean speed $\bar{v} = \Delta d\omega/2\pi$, respectively[1]. Remarkably, one can see that the changes in slippage induce a non-monotonic dependence of both net displacement and mean speed on the frequency. In particular, there exist globally (locally) optimal frequencies for maximizing the net displacement (speed). Figure 9d plots the normalized curvature $\kappa = l\Delta\theta/\Delta d$ as a function of frequency. It can be seen that for the range of no-slip gaits $\omega < 2.7$, the curvature is zero since the gaits have zero net rotation. Moreover, for $\omega = 6.28$, the curvature of the trajectory is maximized.

In order to study the effect of reversal in direction of net motion, we define the projected displacement d_p as the projection of the net displacement vector $\mathbf{\Delta r}_0$ on the mean direction $\bar{\mathbf{e}}_0$ of the central link across a period, and the displacement angle γ is defined as the relative angle between those two vectors (see Figure 8). These two definitions are formally given as

$$d_p = \mathbf{\Delta r}_0 \cdot \bar{\mathbf{e}}_0 \text{ and } \gamma = \cos^{-1}\left(\frac{\mathbf{\Delta r}_0 \cdot \bar{\mathbf{e}}_0}{|\mathbf{\Delta r}_0|}\right), \text{ where}$$

$$\bar{\mathbf{e}}_0 = \begin{pmatrix} \cos\bar{\theta} \\ \sin\bar{\theta} \end{pmatrix}, \bar{\theta} = \frac{1}{t_p}\int_{t_0}^{t_0+t_p} \theta(t)dt, \text{ and } t_p = \frac{2\pi}{\omega}. \tag{21}$$

Figures 9e and 9f plot d_p/l and γ, respectively, as a function of the actuation frequency ω. One can see that the reversal in direction of net displacement occurs at the frequency of $\omega \approx 6.6 \ rad/s$, slightly beyond the

---

[1] Note that for gaits with nonzero net rotation, the net displacement Δd actually depends on the choice of the initial time (phase) of the gait in (9). Nevertheless, for small rotations this dependence has negligible effect, and thus it is not considered here for simplicity.

point where the central wheel slips during the entire period (Figure 9a). Finally, we note that the small gaps in the curves at all plots for $\omega > 9.5$ are due to numerical problems encountered by the event detection function of Matlab's ode45 solver for specific frequencies, under which two or more different transition events occur at very close times.

5.2 Analysis of a singular elliptic gait

We now conduct numerical analysis of the robot's hybrid dynamics under an elliptic gait that passes through singular configurations. The gait is given by (9) with $\alpha_1 = \alpha_2 = 0$, $\beta_1 = 0.25\pi$ and $\beta_2 = 0.3\pi$, and its trajectory in (ϕ_1, ϕ_2)-plane is plotted in Figure 3a (dahsed curve). As an example, Figures 10a-c show plots of the constraint forces $\lambda_i(t)$ and slip velocities $v_i(t)$ along a period, under frequency of $\omega = 4.8 rad/s$. A single period is shown, after convergence to a periodic solution (after six periods). Times where the joint angles pass singular configurations $\phi_1 = \phi_2$ are marked by dotted vertical lines. It can be seen that Coulomb friction bounds and stick-slip transitions ensure that the constraint forces are finite and bounded even at configurations of kinematic singularity. The net displacement of the robot in a period is $\Delta d = 4.6l$. Nevertheless, the net rotation is zero, so that the robot's average motion is along a straight line. This is due to symmetry of the joint angle's motion about zero, which induces constraint forces and slip velocities which are also symmetric about zero. Figure 10d shows the trajectory of the robot's centerpoint $\mathbf{r}_0(t)$ during several periods of the gait. It can be seen that the robot moves in opposite direction (to the left) compared to the shifted circle gaits at low frequencies (Figure 5b). This is in spite of the fact that the two gait trajectories have the same sense of anti-clockwise motion in the plane of joint angles (Figures 3a and 5a). Animation movie of the simulated robot's motion appears in the supplementary information, where the colored blinking arrows denote times and direction of slippage at each wheel.

Next, we conduct numerical simulations while the frequency varies within the range $3 \leq \omega \leq 5.2 rad/s$. Figure 11a plots the percentage of slipping time of each wheel in a period, as a function of frequency. It can be seen that for any frequency, at least one wheel is slipping during the period due to the crossing of singular configurations. Figures 11b and 11c plot the net displacement per period Δd and the mean speed $\bar{v}$, respectively. It can be seen that the net displacement is maximized at an optimal frequency, whereas the mean speed grows monotonically with frequency. No reversal in net direction of motion has been observed for this
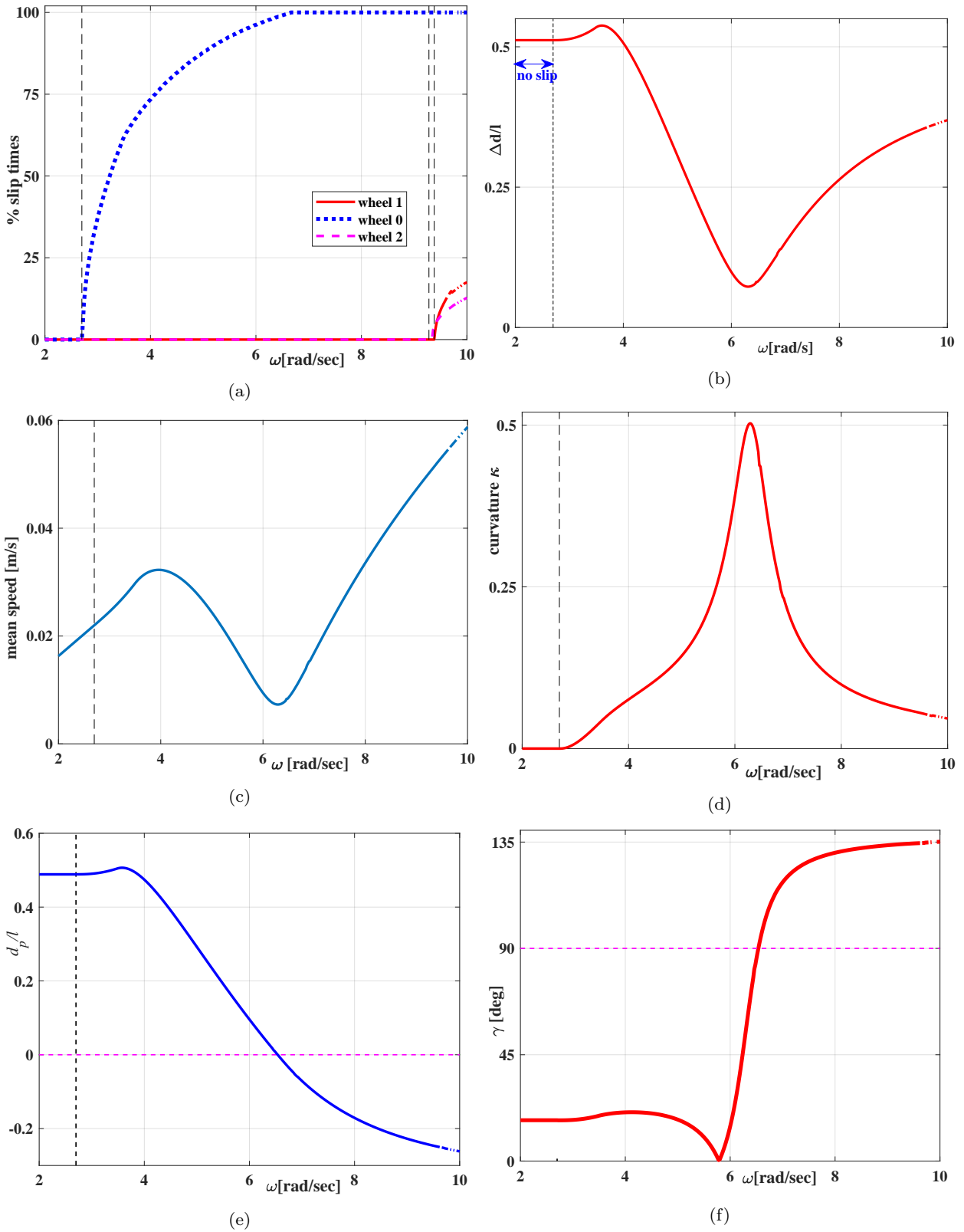
Fig. 9: Quantities of periodic solution under the shifted circle gait as a function of frequency ω: (a) Percentage of slippage time for each wheel. (b) Normalized Net displacement $\Delta d/l$. (c) Mean speed $\bar{v} = 2\pi \Delta d/\omega$. (d) Normalized curvature $\kappa = l\Delta\theta/\Delta d$. (e) Normalized projected displacement d_p/l. (f) TEMP Displacement angle γ.
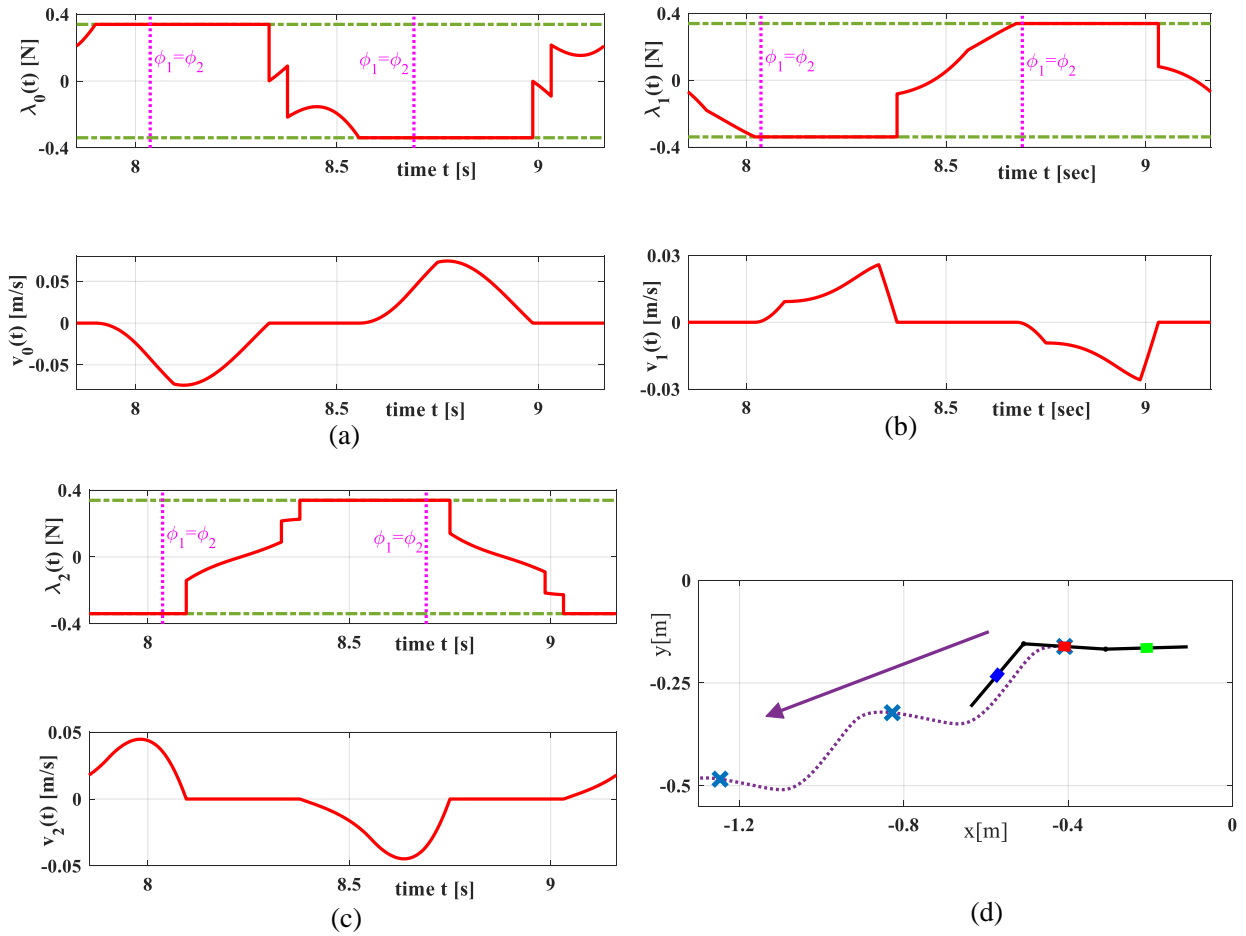
Fig. 10: (a)-(c): Time plots of simulation results for the symmetric ellipse gait with $\omega = 4.8 rad/s$, constraint forces $\lambda_i(t)$ and slip velocities $v_i(t)$. (d) Trajectory of the robot's center $\mathbf{r}_0(t)$ (dotted curve), positions at integer period times are marked by '$\times$'.
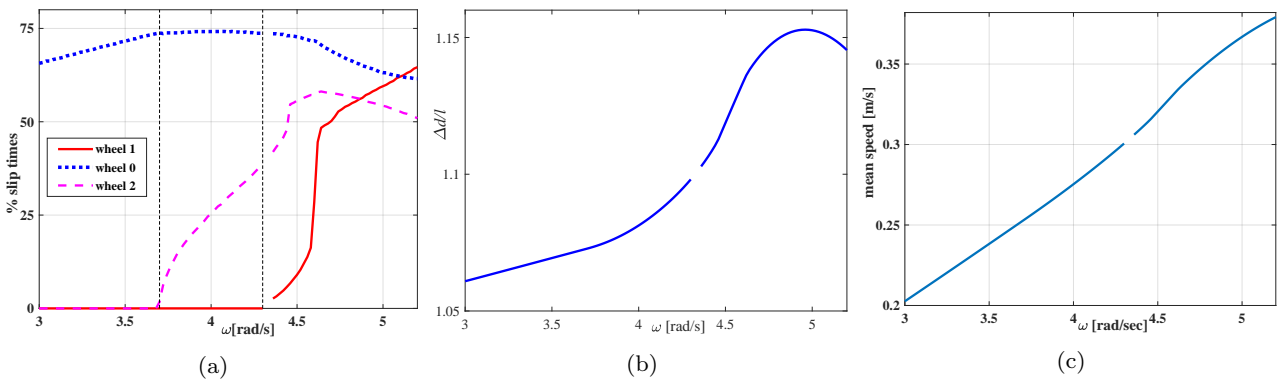

Fig. 11: Quantities of periodic solution under the symmetric ellipse gait as a function of frequency ω: (a) Percentage of slippage time for each wheel. (b) Normalized net displacement $\Delta d/l$. (c) Mean speed $\bar{v} = 2\pi \Delta d/\omega$.

gait ($d_p < 0$ for all ω, plot not shown). Again, the gaps in the plots denote frequencies where the simulation becomes numerically sensitive and fails due to coincidence of two different events. Note that this sensitivity becomes much more severe under the symmetric circle gait, and thus we chose not to use it as a dynamic simulation example in this study.

5.3 Influence of gaits' amplitude

We now study the influence of the input's amplitude and compare between the non-singular shifted circle gait (Figure 5a) and the symmetric ellipse gait (Figure 3a, dashed). Both gaits are given by Eq. (9). The shifted circle gait has $\alpha_2 = -\alpha_1 = 0.45\pi$ and $\beta_1 = \beta_2 = \beta$, whereas the symmetric ellipse gait has $\alpha_1 = \alpha_2 = 0$ and $\beta_2 = 1.2\beta_1 = \beta$. Note that the shift of the circle's center has been increased to 0.45π. This enables examination of gait's amplitudes up to $\beta = 0.5\pi$ without crossing the singularity line $\phi_1 = \phi_2$. On the other hand, the symmetric ellipse gait crosses singularity for any amplitude. Numerical simulations under the two gaits have been conducted for amplitude range of $0 < \beta \leq 0.5\pi \; rad$, for frequency of $\omega = 0.3 rad/s$. This frequency is sufficiently low, so that motion under the non-singular shifted circle gait does not include slippage for all values of β. On the other hand, motion under the ellipse gait always involves slippage during a period. Figure 12a plots the percentage of slipping time of each wheel in a period, as a function of the amplitude β. It can be seen that only the middle wheel 0 is slipping. For low amplitude, where the entire gait trajectory is close to the singularity at origin $\phi_1 = \phi_2 = 0$, the wheel slips during 100% of the period, and the slippage time percentage then decreases when the amplitude is increased. Figure 12b shows a log-log plot of the net displacements per period Δd (after transient time and convergence to periodic motion) under both gaits, as a function of the amplitude β. It can be seen that the elliptic gait achieves significantly larger net displacement for amplitudes up to $\sim 1.2 rad$, above which the shifted circle gait achieves larger net displacements. This might be explained by the large body velocities which are achieved just before reaching friction limits and slippage. In addition, it can be seen that for the shifted circle gait, the net displacements increases as β^2, whereas for the singular gait Δd decreases with β and does not seem to obey any straightforward power law. The explanation for this difference is that under the non-singular circle gait, the no-slip dynamics is regular and smooth, thus for small amplitudes Δd can be approximated using asymptotic expansion in the amplitude β, as done in previous works, cf. [45,13]. On the other hand, the dynamics under the singular ellipse gait involves non-smooth hybrid transitions, and thus it is not amenable to similar asymptotic analysis. Finally, we note that no reversal in the net direction of motion has been observed while varying the gaits' amplitudes.

6 Conclusion

In this paper, we revisited the kinematic model of the wheeled three-link snake and studied its singularities where the nonoholonomic constraints become linearly dependent. We have formulated the model's dynamics and shown that constraint forces and actuation torques grow unbounded upon reaching singular configurations. We have incorporated hybrid dynamics of stick-slip transitions under Coulomb's friction law, and conducted numerical simulations in order to study the influence of actuation frequency under harmonic inputs. For the shifted circle gait which does not pass through singular configurations, there exists a critical frequency above which wheel slippage begins to evolve and the motion rapidly converges to periodic solution. The net displacement per period and mean speed both display non-monotonic dependence on the actuation frequency, having local and/or global extremum points. Additionally, the direction of the robot's net motion reverses its sense with varying frequency. For a gait of symmetric ellipse that passes through singularity, stick-slip transitions occur for any actuation frequency, while the constraint forces remain finite and bounded. Finally, we studied the influence of the gaits' amplitude and compared between a "kinematic gait" of shifted circle without slippage and a symmetric ellipse gait which involves stick-slip transitions. The results show how singularity is resolved by the hybrid model in a physically meaningful way.

We now briefly discuss some limitations of our work and sketch possible directions for future extension of the research. First, in terms of mathematical analysis of our model, one can further study the orbital stability of periodic solutions using hybrid Poincaré map analysis [46,47]. Additionally, one can apply asymptotic expansion in order to find closed-form approximation of net displacements under kinematic (nonsingular) gaits and conduct parametric optimization as in [45,48]. Another open problem is investigating the behavior of the system near kinematic singularities under mechanical input of joint torques rather than torques angle. Our numerical simulation example that appears in Appendix C shows that a singular configuration is reached without unbounded growth of body velocities and constraint forces. This observation is also supported by recent models of mixed kinematic-dynamic variants of the three-wheel snake [43], [44].
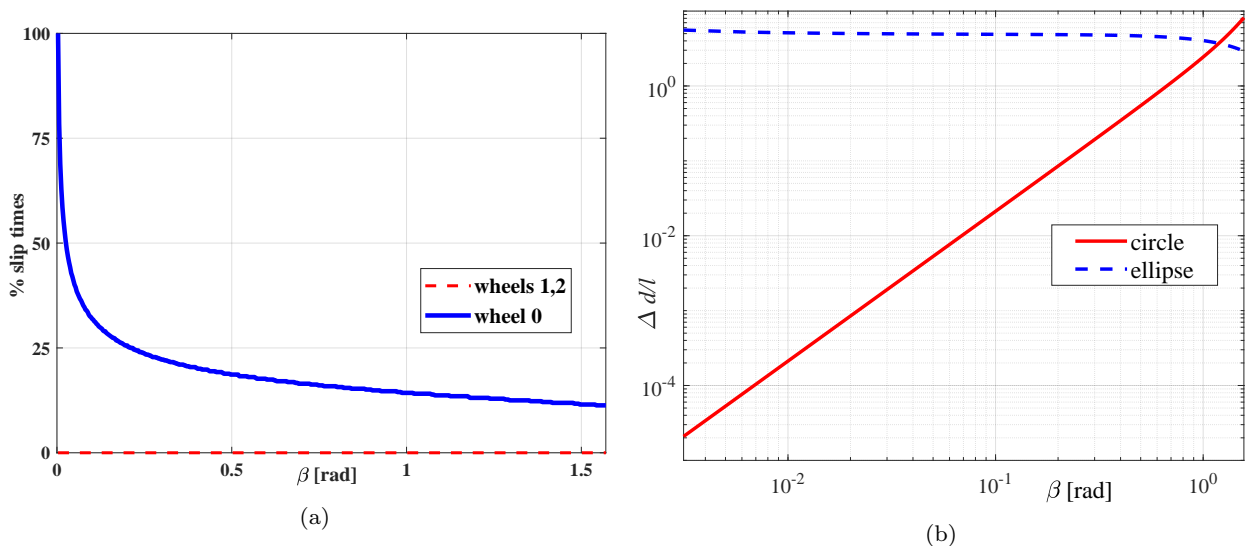
Fig. 12: Comparison between gaits of shifted circle and symmetric ellipse under frequency $\omega = 0.3 rad/s$, as a function of gaits' amplitude β: (a) Percentage of slippage time for each wheel (ellipse only). (b) Normalized net displacements in period $\Delta d/l$.

Second, our friction model is simplified since it assumes that the normal forces N_i are constant. This holds only when the height of the center of mass is negligible $\Delta z \ll l$, see Figure 1b. Relaxing this assumption, the normal forces become coupled to the center-of-mass accelerations. This coupling is complicated since it involves $3D$ rotational dynamics of the robot. A third possible extension is comparison with smooth models of slippage and friction such as the "slip-angle" model [27–30].

As mentioned above, an evident limitation of our numerical analysis is its sensitivity of the chosen integration scheme which causes failure in particular cases where different events occur at very close times (see small gaps in the plots in Figures 11b, 11c, and 9a). Using alternative integration schemes for stiff and piecewise-smooth systems [49–51] is another open challenge. Finally, in a near future work we plan to experimentally validate our friction model and its theoretical analysis via motion measurements of controlled robotic prototypes of the three-wheel snake.

Conflicts of Interest and Funding: The authors declare that they have no conflict of interest. No funding has been received to support this research.

Appendix A - dimensional analysis of the dynamics and scaling with actuation frequency

Consider the constrained dynamical system in (14), combined with the time-derivative of the constraints in (15).

The body acceleration can be obtained from (14) as

$$\ddot{\mathbf{q}}_b = \mathbf{M}_{bb}^{-1}(\mathbf{W}_b^T \boldsymbol{\Lambda} - \mathbf{M}_{bs}\ddot{\mathbf{q}}_s - \mathbf{B}_b). \tag{22}$$

Substituting (22) into (15), an explicit expression for the vector $\boldsymbol{\Lambda}$ of constraint forces is obtained as:

$$\boldsymbol{\Lambda} = \left(\mathbf{W}_b\mathbf{M}_{bb}^{-1}\mathbf{W}_b^T\right)^{-1}\left(\mathbf{W}_b\mathbf{M}_{bb}^{-1}(\mathbf{M}_{bs}\ddot{\mathbf{q}}_s + \mathbf{B}_b)\right.$$
$$\left. - \mathbf{W}_s\ddot{\mathbf{q}}_s - \dot{\mathbf{W}}_b\dot{\mathbf{q}}_b\right) \tag{23}$$

Next, consider a periodic gait input $\mathbf{q}_b(t)$ of the form (9), with a variable actuation frequency ω. The shape velocity and acceleration vectors thus scale as $\dot{\mathbf{q}}_s \sim \omega$ and $\ddot{\mathbf{q}}_s \sim \omega^2$. Assuming that the gait does not cross any singularity $\det(\mathbf{W}_b) \neq 0$, the kinematic relation (6) implies that the body velocity scales as $\dot{\mathbf{q}}_b \sim \omega$, and (15) implies that $\ddot{\mathbf{q}}_b \sim \omega^2$. Finally, the velocity-dependent vector $\mathbf{B}_b(\mathbf{q}, \dot{\mathbf{q}})$ and matrices $\dot{\mathbf{W}}_b, \dot{\mathbf{W}}_s$ are quadratic in the velocities $\dot{\mathbf{q}}$, and thus scale as ω^2. Therefore, (23) implies that the vector $\boldsymbol{\Lambda}$ of constraint forces scales as ω^2.

Appendix B - singularity analysis of the hybrid dynamics

We now analyze the conditions for singularity in the dynamics of all possible combinations of stick-slip states. The dynamic equations of motion are given in (14), which gives 5 scalar equations. These equations are augmented by (20), giving rise to a 8×8 linear system of the form $\mathbf{Az} = \mathbf{b}$ where the vector of unknowns is
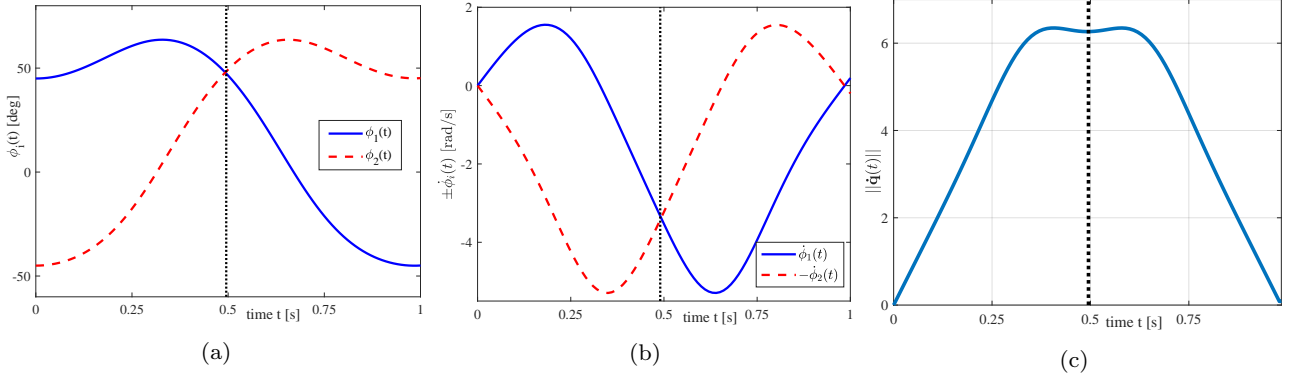
Fig. 13: Time plots of simulation results under torque input: (a) Joint angles $\phi_i(t)$. (b) Joint velocities $\pm\dot{\phi}_i(t)$. (c) Norm of velocity $||\dot{\mathbf{q}}(t)||$.

$\mathbf{z} = (\ddot{\mathbf{q}}_b, \boldsymbol{\tau}, \boldsymbol{\Lambda})$. This can be further simplified by direct substitution of the constraint force λ_i for each slipping wheel from (20), and eliminating λ_i from the vector $\mathbf{z}$. This reduces the dimension of the linear system to $8 - n_s$ where n_s is the number of slipping wheels. We then calculate the determinant D of the linear system's $(8-n_s) \times (8-n_s)$ matrix and analyze the conditions for $D = 0$, which is a singularity of the dynamics. In the following, we repeat this process for all possible combinations of stick-slip states, while disregarding symmetries between the two side links $i = 1, 2$. We use the abbreviations $c_i = \sin\phi_i$, $s_i = \cos\phi_i$ for $i = 1, 2$. First, consider the case of only wheel 1 slipping. The determinant D is obtained as:

$$D = \frac{m_1 l^2}{3}\left(3\eta - 6s_1 s_2 - 2c_2^2 + 2\eta^3 c_2^2 + 6\eta c_1 + 12\eta c_2 \right.$$
$$\left. + 6\eta^2 + \eta^3 + 6\eta^2 c_2 - 6\eta c_1 c_2^2 - 6\eta c_2 s_1 s_2 + 8\right).$$

It can be shown that the minimal value of D is zero, which is attained only for $\eta = 1$ and $\phi_2 = \pm\pi$. These values of joint angle are nonphysical, due to collision between links and coincidence of wheels 0 and 2.

Second, consider the case of only wheel 0 slipping. The determinant D is obtained as:

$$D = \frac{m_1 l^2}{3}\left(6\eta + 2\cos(2\phi_1 + 2\phi_2) + 12\cos(\phi_1 + \phi_2)\right.$$
$$+ 3\eta^2 \cos(\phi_1 + 2\phi_2) + 3\eta^2 \cos(2\phi_1 + \phi_2) + 6\eta^2 \cos(2\phi_1)$$
$$+ 6\eta^2 \cos(2\phi_2) + 3\eta^3 \cos(2\phi_1) + 3\eta^3 \cos(2\phi_2)$$
$$+ 6\eta\cos(\phi_1 + \phi_2) + \eta^3 \cos(2\phi_1 + 2\phi_2) + 18\eta\cos(\phi_1)$$
$$+ 18\eta\cos(\phi_2) + 12\eta^2 + 5\eta^3 + 6\eta\cos(\phi_1 + 2\phi_2)$$
$$\left. + 6\eta\cos(2\phi_1 + \phi_2) + 9\eta^2 \cos(\phi_1) + 9\eta^2 \cos(\phi_2) + 10\right)$$

Setting $D = 0$, it can be shown that singularity occurs when $\phi_1 + \phi_2 = \pm\pi$ or when $\phi_1, \phi_2 = \pm\pi$.

Next, consider the case where wheels 1 and 2 are both slipping. The determinant D is obtained as:

$$D = \frac{m_1^2 l^2}{3}\left(8\eta - 6s_1 s_2 + 3c_1^2 + 3c_2^2 + 12\eta c_1 + 12\eta c_2 \right.$$
$$\left. + 12\eta^2 + 8\eta^3 + \eta^4 + 6\eta^2 c_1 + 6\eta^2 c_2 + 10\right).$$

The minimal value of $D_{min} = \frac{4m_1^2 l^2}{3} > 0$ is obtained in the nonphysical case of $\eta = 0$, for $\phi_1 = \phi_2 = \pi/2$.

Now consider the case where wheels 0 and 1 are both slipping. The determinant D is obtained as:

$$D = \frac{m_1^2 l^2}{6}\left(28\eta + 3\cos(2\phi_1 + 2\phi_2) + 24\cos(\phi_1 + \phi_2)\right.$$
$$+ 6\eta^2 \cos(\phi_1 + 2\phi_2) + 12\eta^2 \cos(2\phi_2) + 12\eta^3 \cos(2\phi_2)$$
$$+ 3\eta^4 \cos(2\phi_2) + 12\eta\cos(\phi_1 + \phi_2) + 36\eta\cos(\phi_1)$$
$$+ 48\eta\cos(\phi_2) + 42\eta^2 + 28\eta^3 + 5\eta^4 + 12\eta\cos(\phi_1 + 2\phi_2)$$
$$\left. + 18\eta^2 \cos(\phi_1) + 48\eta^2 \cos(\phi_2) + 12\eta^3 \cos(\phi_2) + 29\right).$$

The minimal value of $D_{min} = \frac{4m_1^2 l^2}{3}$ is obtained in the nonphysical case of $\eta = 0$, for $\phi_1 + \phi_2 = \pi$.

Finally, consider the case where all three wheels are slipping. The determinant D is obtained as:

$$D = \frac{m_1^3 l^2}{3}(\eta + 2)\left(8\eta + 6\cos(\phi_1 + \phi_2) + 12\eta c_1 + 12\eta c_2 + 12\eta^2\right.$$
$$\left. + 8\eta^3 + \eta^4 + 6\eta^2 c_1 + 6\eta^2 c_2 + 10\right).$$

The minimal value of $D_{min} = \frac{8m_1^3 l^2}{3}$ is obtained in the nonphysical case of $\eta = 0$, for $\phi_1 + \phi_2 = \pi$.

Appendix C - dynamics under torque input near singularity

Consider the three-wheel snake robot as a constrained nonholonomic mechanical system where the torques $\boldsymbol{\tau}(t)$ are the controlled input while the shape variables $\mathbf{q}_s$ are evolving dynamically. The system'e equations of motion (14) and (15) give rise to a 8×8 linear system

of the form $\mathbf{A}\mathbf{z} = \mathbf{b}$ where the vector of unknowns is $\mathbf{z} = (\ddot{\mathbf{q}}_b, \ddot{\mathbf{q}}_s, \boldsymbol{\Lambda})$. The determinant of this system can be obtained as:

$$D = \tfrac{1}{9}m_1 l^6 \eta^2 \left(16\eta - 2\cos(2\phi_1 - 2\phi_2) + 3\eta^2\right.$$

$$\left. -2\eta\cos(2\phi_1) - 2\eta\cos(2\phi_2) + 14\right).$$

It can be shown that the minimal value of D is obtained for $\phi_1 = \phi_2 = 0$ as

$$D_{min} = \frac{1}{3}m_1 l^6 \eta^2 (\eta + 2)^2 > 0.$$

This implies that the dynamical system is never singular, so that $(\ddot{\mathbf{q}}_b, \ddot{\mathbf{q}}_s, \boldsymbol{\Lambda})$ are always finite and bounded. Nevertheless, if the system is driven into a configuration of kinematic singularity where $\det(\mathbf{W}_b) = 0$, the body velocity $\mathbf{q}_b$ may still grow unbounded according to (6).

We now examine this case in a numerical simulation under torque input. Physical parameters of the robot are chosen as $l = h = 0.1m$ and $m_0 = m_1 = m_2 = 0.17Kg$. Initial conditions are chosen as $\mathbf{q}_b(0) = 0$, $\phi_1(0) = -\phi_2(0) = 0.25\pi$ and $\dot{\mathbf{q}}(0) = 0$. The joint torques are constant: $\tau_1 = \tau_2 = 0.05\ N \cdot mm$. That is, the torques drive the system towards a singular configuration where $\phi_1 = \phi_2$. Simulation results of the joint angles $\phi_i(t)$ and their velocities $\pm\dot{\phi}_i(t)$ are plotted in Figures 13a and 13b, respectively. It can be seen that the system reaches a configuration of kinematic singularity $\phi_1 = \phi_2$ at time $t_s \approx 0.49s$, marked as dotted vertical line. Interestingly, at the same time the joints' angular velocities are driven to satisfy $\dot{\phi}_1 = -\dot{\phi}_2$, which is precisely the condition given in (8) for bypassing the kinematic singularity. Figure 13c shows a time plot of the velocity norm $||\dot{\mathbf{q}}(t)||$, indicating that, indeed, it remains finite and bounded. That is, the system is driven passively towards bypassing the kinematic singularity without divergence.

References

1. A. Bloch, J. Baillieul, P. Crouch, J. E. Marsden, D. Zenkov, P. S. Krishnaprasad, and R. M. Murray, *Nonholonomic mechanics and control*. Springer, 2003, vol. 24.
2. J. I. Neimark and N. A. Fufaev, *Dynamics of nonholonomic systems*. American Mathematical Soc., 2004, vol. 33.
3. S. Chaplygin, "Collected works. vol. 3. the theory of the motion of non-holonomic systems: Examples of the use of the reducing factor method," 1950.
4. S. Stanchenko, "Non-holonomic Chaplygin systems," *Journal of Applied Mathematics and Mechanics*, vol. 53, no. 1, pp. 11–17, 1989.
5. A. M. Bloch, P. Krishnaprasad, J. E. Marsden, and R. M. Murray, "Nonholonomic mechanical systems with symmetry," *Archive for Rational Mechanics and Analysis*, vol. 136, no. 1, pp. 21–99, 1996.
6. J. Ostrowski, A. Lewis, R. Murray, and J. Burdick, "Nonholonomic mechanics and locomotion: the snakeboard example," in *Robotics and Automation, 1994. Proceedings., 1994 IEEE International Conference on*. IEEE, 1994, pp. 2391–2397.
7. P. Krishnaprasad and D. P. Tsakiris, "Oscillations, se (2)-snakes and motion control: A study of the roller racer," *Dynamical Systems: An International Journal*, vol. 16, no. 4, pp. 347–397, 2001.
8. F. Bullo and M. Žefran, "On mechanical control systems with nonholonomic constraints and symmetries," *Systems & Control Letters*, vol. 45, no. 2, pp. 133–143, 2002.
9. S. Chitta, P. Cheng, E. Frazzoli, and V. Kumar, "Robotrikke: A novel undulatory locomotion system," in *Robotics and Automation, 2005. ICRA 2005. Proceedings of the 2005 IEEE International Conference on*. IEEE, 2005, pp. 1597–1602.
10. S. Chitta and V. Kumar, "Dynamics and generation of gaits for a planar rollerblader," in *Intelligent Robots and Systems, 2003.(IROS 2003). Proceedings. 2003 IEEE/RSJ International Conference on*, vol. 1. IEEE, 2003, pp. 860–865.
11. S. D. Kelly and R. M. Murray, "Geometric phases and robotic locomotion," *Journal of Field Robotics*, vol. 12, no. 6, pp. 417–431, 1995.
12. J. Ostrowski and J. Burdick, "The geometric mechanics of undulatory robotic locomotion," *The International Journal of Robotics Research*, vol. 17, no. 7, pp. 683–701, 1998.
13. O. Chakon and Y. Or, "Analysis of underactuated dynamic locomotion systems using perturbation expansion: The twistcar toy example," *Journal of Nonlinear Science*, vol. 27, no. 4, pp. 1215–1234, 2017.
14. E. A. Shammas, H. Choset, and A. A. Rizzi, "Geometric motion planning analysis for two classes of underactuated mechanical systems," *The International Journal of Robotics Research*, vol. 26, no. 10, pp. 1043–1073, 2007.
15. Y. Nakamura, H. Ezaki, Y. Tan, and W. Chung, "Design of steering mechanism and control of nonholonomic trailer systems," *IEEE transactions on Robotics and Automation*, vol. 17, no. 3, pp. 367–374, 2001.
16. D. Tilbury, R. M. Murray, and S. S. Sastry, "Trajectory generation for the N-trailer problem using Goursat normal form," *IEEE Transactions on Automatic Control*, vol. 40, no. 5, pp. 802–819, 1995.
17. R. L. Hatton and H. Choset, "Geometric swimming at low and high Reynolds numbers," *IEEE Transactions on Robotics*, vol. 29, no. 3, pp. 615–624, 2013.
18. F. Alouges, A. DeSimone, L. Giraldi, and M. Zoppello, "Self-propulsion of slender micro-swimmers by curvature control: N-link swimmers," *International Journal of Non-Linear Mechanics*, vol. 56, pp. 132–141, 2013.
19. E. Kanso, J. E. Marsden, C. W. Rowley, and J. B. Melli-Huber, "Locomotion of articulated bodies in a perfect fluid," *Journal of Nonlinear Science*, vol. 15, no. 4, pp. 255–289, 2005.
20. T. Miloh and A. Galper, "Self-propulsion of general deformable shapes in a perfect fluid," *Proc. R. Soc. Lond. A*, vol. 442, no. 1915, pp. 273–299, 1993.
21. E. Gutman and Y. Or, "Symmetries and gaits for Purcell's three-link microswimmer model," *IEEE Transactions on Robotics*, vol. 32, no. 1, pp. 53–69, 2016.
22. J. B. Melli, C. W. Rowley, and D. S. Rufat, "Motion planning for an articulated body in a perfect planar fluid," *SIAM Journal on applied dynamical systems*, vol. 5, no. 4, pp. 650–669, 2006.

23. E. Kanso and J. E. Marsden, "Optimal motion of an articulated body in a perfect fluid," in *Decision and Control, 2005 and 2005 European Control Conference. CDC-ECC'05. 44th IEEE Conference on.* IEEE, 2005, pp. 2511–2516.

24. D. Tam and A. E. Hosoi, "Optimal stroke patterns for Purcell's three-link swimmer," *Physical Review Letters*, vol. 98, no. 6, p. 068105, 2007.

25. O. Wiezel and Y. Or, "Using optimal control to obtain maximum displacement gait for Purcell's three-link swimmer," in *Decision and Control (CDC), 2016 IEEE 55th Conference on.* IEEE, 2016, pp. 4463–4468.

26. R. M. Murray, Z. Li, and S. S. Sastry, *A Mathematical Introduction to Robotic Manipulation.* Boca Raton, FA: CRC Press, 1994.

27. N. Sidek and N. Sarkar, "Dynamic modeling and control of nonholonomic mobile robot with lateral slip," in *Systems, 2008. ICONS 08. Third International Conference on.* IEEE, 2008, pp. 35–40.

28. S. Bazzi, E. Shammas, D. Asmar, and M. T. Mason, "Motion analysis of two-link nonholonomic swimmers," *Nonlinear Dynamics*, vol. 89, no. 4, pp. 2739–2751, 2017.

29. H. Salman, T. Dear, S. Babikian, E. Shammas, and H. Choset, "A physical parameter-based skidding model for the snakeboard," in *Decision and Control (CDC), 2016 IEEE 55th Conference on.* IEEE, 2016, pp. 7555–7560.

30. Y. Tian, N. Sidek, and N. Sarkar, "Modeling and control of a nonholonomic wheeled mobile robot with wheel slip dynamics," in *Computational Intelligence in Control and Automation, 2009. CICA 2009. IEEE Symposium on.* IEEE, 2009, pp. 7–14.

31. T. Dear, S. D. Kelly, M. Travers, and H. Choset, "Snakeboard motion planning with viscous friction and skidding," in *Robotics and Automation (ICRA), 2015 IEEE International Conference on.* IEEE, 2015, pp. 670–675.

32. V. Fedonyuk and P. Tallapragada, "Stick–slip motion of the Chaplygin sleigh with a piecewise-smooth nonholonomic constraint," *Journal of Computational and Nonlinear Dynamics*, vol. 12, no. 3, p. 031021, 2017.

33. P. Cheng, E. Frazzoli, and V. Kumar, "Motion planning for the roller racer with a sticking/slipping switching model," in *Robotics and Automation, 2006. ICRA 2006. Proceedings 2006 IEEE International Conference on.* IEEE, 2006, pp. 1637–1642.

34. K. Zadarnowska and A. Oleksy, "Motion planning of wheeled mobile robots subject to slipping," *Journal of Automation Mobile Robotics and Intelligent Systems*, vol. 5, pp. 49–58, 2011.

35. A. Tarakameh, K. Shojaei, and A. M. Shahri, "Adaptive control of nonholonomic wheeled mobile robot in presence of lateral slip and dynamic uncertainties," in *Electrical Engineering (ICEE), 2010 18th Iranian Conference on.* IEEE, 2010, pp. 592–598.

36. Y. Tian, S. N. Sidek, and N. Sarkar, "Tracking control for nonholonomic wheeled mobile robot with wheel slip dynamics," in *ASME 2009 Dynamic Systems and Control Conference.* American Society of Mechanical Engineers, 2009, pp. 739–746.

37. S. Nandy, S. Shome, R. Somani, T. Tanmay, G. Chakraborty, and C. Kumar, "Detailed slip dynamics for nonholonomic mobile robotic system," in *Mechatronics and Automation (ICMA), 2011 International Conference on.* IEEE, 2011, pp. 519–524.

38. A. A. Transeth, K. Y. Pettersen, and P. Liljebäck, "A survey on snake robot modeling and locomotion," *Robotica*, vol. 27, no. 7, pp. 999–1015, 2009.

39. P. S. Krishnaprasad and D. P. Tsakiris, "G-snakes: Nonholonomic kinematic chains on lie groups," in *Decision and Control, 1994., Proceedings of the 33rd IEEE Conference on*, vol. 3. IEEE, 1994, pp. 2955–2960.

40. F. Matsuno and K. Suenaga, "Control of redundant 3D snake robot based on kinematic model," in *Robotics and Automation, 2003. Proceedings. ICRA'03. IEEE International Conference on*, vol. 2. IEEE, 2003, pp. 2061–2066.

41. F. Matsuno and H. Sato, "Trajectory tracking control of snake robots based on dynamic model," in *Robotics and Automation, 2005. ICRA 2005. Proceedings of the 2005 IEEE International Conference on.* IEEE, 2005, pp. 3029–3034.

42. M. Tanaka and K. Tanaka, "Singularity analysis of a snake robot and an articulated mobile robot with unconstrained links," *IEEE Transactions on Control Systems Technology*, vol. 24, no. 6, pp. 2070–2081, 2016.

43. T. Dear, S. D. Kelly, M. Travers, and H. Choset, "The three-link nonholonomic snake as a hybrid kinodynamic system," in *American Control Conference (ACC), 2016.* IEEE, 2016, pp. 7269–7274.

44. ——, "Locomotive analysis of a single-input three-link snake robot," in *Decision and Control (CDC), 2016 IEEE 55th Conference on.* IEEE, 2016, pp. 7542–7547.

45. O. Wiezel and Y. Or, "Optimization and small-amplitude analysis of Purcell's three-link microswimmer model," *Proc. R. Soc. A*, vol. 472, no. 2192, p. 20160425, 2016.

46. E. D. Wendel and A. D. Ames, "Rank properties of Poincaré maps for hybrid systems with applications to bipedal walking," in *Proceedings of the 13th ACM international conference on Hybrid systems: computation and control.* ACM, 2010, pp. 151–160.

47. B. Gamus and Y. Or, "Dynamic bipedal walking under stick-slip transitions," *SIAM Journal on Applied Dynamical Systems*, vol. 14, no. 2, pp. 609–642, 2015.

48. E. Gutman and Y. Or, "Optimizing an undulating magnetic microswimmer for cargo towing," *Physical Review E*, vol. 93, no. 6, p. 063105, 2016.

49. L. F. Shampine and C. W. Gear, "A user's view of solving stiff ordinary differential equations," *SIAM review*, vol. 21, no. 1, pp. 1–17, 1979.

50. V. Acary and B. Brogliato, *Numerical methods for nonsmooth dynamical systems: applications in mechanics and electronics.* Springer Science & Business Media, 2008.

51. M. Bernardo, C. Budd, A. R. Champneys, and P. Kowalczyk, *Piecewise-smooth dynamical systems: theory and applications.* Springer Science & Business Media, 2008, vol. 163.